The Astrophysical Journal Supplement Series, 271:41 (15pp), 2024 April https://doi.org/10.3847/1538-4365/ad24fa

S-PLUS: Photometric Recalibration with the Stellar Color Regression Method and an Improved Gaia XP Synthetic Photometry Method

Kai Xiao[1,2], Yang Huang[1,3], Haibo Yuan[2,4], Timothy C. Beers[5], Bowen Huang[2,4], Shuai Xu[2,4], Lin Yang[6], Felipe Almeida-Fernandes[7], Hélio D. Perottoni[8], Guilherme Limberg[7,9,10], William Schoenell[11], Tiago Ribeiro[12], Antonio Kanaan[13], and Natanael Gomes de Oliveira[14]

[1] School of Astronomy and Space Science, University of Chinese Academy of Sciences, Beijing 100049, People's Republic of China; huangyang@ucas.ac.cn
[2] Institute for Frontiers in Astronomy and Astrophysics, Beijing Normal University, Beijing 102206, People's Republic of China; yuanhb@bnu.edu.cn
[3] CAS Key Lab of Optical Astronomy, National Astronomical Observatories, Chinese Academy of Sciences, Beijing 100012, People's Republic of China
[4] Department of Astronomy, Beijing Normal University, Beijing 100875, People's Republic of China
[5] Department of Physics and Astronomy and JINA Center for the Evolution of the Elements (JINA-CEE), University of Notre Dame, Notre Dame, IN 46556, USA
[6] Department of Cyber Security, Beijing Electronic Science and Technology Institute, Beijing 100070, People's Republic of China
[7] Universidade de São Paulo, Instituto de Astronomia, Geofísica e Ciências Atmosféricas, Departamento de Astronomia, SP 05508-090, São Paulo, Brazil
[8] Nicolaus Copernicus Astronomical Center, Polish Academy of Sciences, ul. Bartycka 18, 00-716, Warsaw, Poland
[9] Department of Astronomy & Astrophysics, University of Chicago, 5640 S. Ellis Ave., Chicago, IL 60637, USA
[10] Kavli Institute for Cosmological Physics, University of Chicago, 5640 S. Ellis Ave., Chicago, IL 60637, USA
[11] GMTO Corporation, 465 N. Halstead St., Suite 250, Pasadena, CA 91107, USA
[12] Rubin Observatory Project Office, 950 N. Cherry Ave., Tucson, AZ 85719, USA
[13] Departamento de Física, Universidade Federal de Santa Catarina, Florianópolis, SC 88040-900, Brazil
[14] Valongo Observatory, Federal University of Rio de Janeiro, Rio de Janeiro, 2008090, Brazil
Received 2023 September 24; revised 2024 January 24; accepted 2024 January 24; published 2024 March 21

Abstract

We present a comprehensive recalibration of narrowband/medium-band and broadband photometry from the Southern Photometric Local Universe Survey (S-PLUS) by leveraging two approaches: an improved Gaia XP synthetic photometry (XPSP) method with corrected Gaia XP spectra, and the stellar color regression (SCR) method with corrected Gaia Early Data Release 3 photometric data and spectroscopic data from LAMOST Data Release 7. Through the use of millions of stars as standards per band, we demonstrate the existence of position-dependent systematic errors, up to 23 mmag for the main survey region, in the S-PLUS iDR4 photometric data. A comparison between the XPSP and SCR methods reveals minor differences in zero-point offsets, typically within the range of 1–6 mmag, indicating the accuracy of the recalibration, and a twofold to threefold improvement in the zero-point precision. During this process, we also verify and correct for systematic errors related to CCD position. The corrected S-PLUS iDR4 photometric data will provide a solid data foundation for conducting scientific research that relies on high-precision calibration. Our results underscore the power of the XPSP method in combination with the SCR method, showcasing their effectiveness in enhancing calibration precision for wide-field surveys when combined with Gaia photometry and XP spectra, to be applied for other S-PLUS subsurveys.

Unified Astronomy Thesaurus concepts: Stellar photometry (1620); Astronomy data analysis (1858); Calibration (2179)

1. Introduction

Accurate and uniform photometric calibration presents a challenging task, yet it is crucial for wide-field surveys due to rapid fluctuations in Earth's atmospheric opacity on timescales of seconds to minutes, instrumental effects (e.g., flat-field corrections), and electronics instability (e.g., variation in detector gain over time). Traditional optical photometric calibration relies on networks of standard stars with well-determined photometry, such as those of Landolt (1992, 2009, 2013) and Stetson (2000). However, the limited number of standard stars hinders traditional methods from meeting the calibration accuracy expectations of modern wide-field photometric surveys.

Over the past two decades, significant advancements have been made in achieving high-precision calibration using various methods, broadly categorized into "hardware-driven" and "software-driven" approaches, as discussed by Huang & Yuan (2022). Hardware-driven methods include the ubercalibration method (Padmanabhan et al. 2008), the hypercalibration method (Finkbeiner et al. 2016), and the forward global calibration method (Burke et al. 2018). Software-driven approaches involve techniques such as the stellar locus regression method (High et al. 2009), the stellar color regression (SCR) method (Yuan et al. 2015), and the stellar locus method (López-Sanjuan et al. 2019).

The central idea of the SCR method is to predict the intrinsic colors of stars by utilizing stellar atmospheric parameters, which has proven to be particularly effective in the photometric recalibration of wide-field surveys. For instance, when applied to Sloan Digital Sky Survey (SDSS; York et al. 2000) Stripe 82 (Ivezić et al. 2007), it achieved a precision of 2–5 mmag in the SDSS colors. Additionally, it has been employed for data from Gaia Data Release 2 (Gaia Collaboration et al. 2018) and Early Data Release 3 (EDR3; Gaia Collaboration et al. 2021a, 2021b) to correct for magnitude/color-dependent systematic errors in the Gaia photometry (Niu et al. 2021a, 2021b), yielding an unprecedented precision of 1 mmag.

Huang et al. (2021) utilized the SCR approach to recalibrate the second data release of the SkyMapper Southern Survey (SMSS; Wolf et al. 2018), revealing large zero-point offsets in the u and v bands. Huang & Yuan (2022) applied the method to SDSS Stripe 82 standard-star catalogs (Ivezić et al. 2007; Thanjavur et al. 2021), achieving a precision of 5 mmag in the SDSS u band and of 2 mmag in the $griz$ bands (Yuan et al. 2015). In addition, Xiao & Yuan (2022) and Xiao et al. (2023b) applied the SCR method to the Pan-STARRS1 (PS1; Tonry et al. 2012) data, effectively correcting for significant large-scale and small-scale spatial variations in the magnitude offsets and magnitude-dependent systematic errors. Other applications include that of Xiao et al. (2023c), who used the SCR method to perform recalibration on the J-PLUS Data Release 3 (DR3) photometric data, accurately measuring and correcting for PS1 systematic errors and metallicity-dependent systematic errors present in the data. Xiao et al. (2023a) also performed photometric calibration of the Nanshan 1 m wide-field telescope gri-band imaging data of the Stellar Abundance and Galactic Evolution Survey (SAGES; Zheng et al. 2018, 2019) using the SCR method, achieving 1–2 mmag precision in the zero-points.

Recently, Gaia DR3 (Carrasco et al. 2021; Gaia Collaboration et al. 2023) was released, which provides ultra-low-resolution ($\lambda/\Delta\lambda \sim 50$) BP/RP (XP) spectra for roughly 220 million sources, with the majority having magnitudes $G < 17.65$. The XP spectra cover wavelengths from 336 to 1020 nm, and have undergone precise internal (Carrasco et al. 2021; De Angeli et al. 2023) and external calibrations (Montegriffo et al. 2023). Unfortunately, the Gaia XP spectra exhibit systematic errors that depend on magnitude and color, particularly at wavelengths below 400 nm (see, e.g., Montegriffo et al. 2023; Huang et al. 2024).

More recently, comprehensive corrections to the Gaia XP spectra have been provided by Huang et al. (2024), utilizing spectra from CALSPEC (Bohlin et al. 2014; Bohlin & Lockwood 2022) and Hubble's Next Generation Spectral Library (NGSL; Koleva & Vazdekis 2012). In this process, the spectroscopy-based SCR method (Yuan et al. 2015) was employed as well. Based on the corrected Gaia XP spectra, Xiao et al. (2023c) further developed the XP spectra–based photometric synthesis (XPSP) method, and applied it to the photometric calibration of J-PLUS DR3 data. The consistency between the J-PLUS zero-points predicted by the XPSP method after XP spectrum correction and the SCR method is better than 5 mmag, which represents a twofold improvement as compared to the consistency between the J-PLUS zero-points predicted by the XPSP method with uncorrected XP spectra and the SCR method.

Conducted at the Cerro Tololo Inter-American Observatory, the Southern Photometric Local Universe Survey (S-PLUS[15]; Mendes de Oliveira et al. 2019) employs an 83 cm telescope to obtain images on a single CCD. The photometric calibration of S-PLUS Internal Data Release 4 (iDR4) is carried out using photometric data from the Galaxy Evolution Explorer, SDSS, Pan-STARRS, SkyMapper, and so on, along with spectral energy distribution (SED) information for calibration sources (Almeida-Fernandes et al. 2022). However, this method (i) relies on reference catalogs that do not have uniform calibration precision across the S-PLUS footprint; (ii) relies on synthetic stellar models, and will inherit any systematic errors present in these (for instance, Almeida-Fernandes et al. 2022 observed zero-point offsets as high as 50 mmag for the $J0395$ band just by changing the synthetic spectral library); (iii) relies on the Schlegel et al. (1998) extinction maps, and thus fails at low Galactic latitudes, and exhibits spatially dependent systematic errors, up to 0.02 mag (Sun et al. 2022); and (iv) uses aperture corrections for the determination of aperture magnitudes. Improvement of the photometric calibration of S-PLUS is crucial, given the importance of high-precision investigations, particularly those that seek accurate determinations of stellar parameters and elemental abundances.

In this study, we utilize both an improved XPSP method and the SCR method to conduct photometric recalibration of the S-PLUS iDR4 data (F. R. Herpich et al. 2024, in preparation), aiming to achieve uniform photometry with accuracy better than 1%. The structure of this paper is as follows. We present the data used in this work in Section 2. Predictions of the S-PLUS magnitudes with the XPSP method and the SCR method are presented in Section 3, followed by a description of systematic errors present in the S-PLUS iDR4 data in Section 4. A discussion is carried out in Section 5. Finally, we provide brief conclusions in Section 6.

2. Data

2.1. S-PLUS iDR4

S-PLUS iDR4 encompasses 1629 pointings with both aperture photometry (PStotal) and point-spread function (PSF) photometry, covering approximately 3000 deg^2 of the southern sky, including the main survey with PStotal and PSF photometry, the Magellanic Clouds (MCs) with PStotal and PSF photometry, and the disk survey with PSF photometry (F. R. Herpich et al. 2024, in preparation). The PStotal photometry was the one used for calibration, and is the best representation of the total magnitude of a point source in the S-PLUS catalogs (for the aperture photometry). The S-PLUS data were obtained using the T80-South telescope.[16] The panoramic camera features a single charge-coupled device (CCD) with 9.2k × 9.2k pixels, a field of view measuring $1\overset{\circ}{.}4 \times 1\overset{\circ}{.}4$, and a pixel scale of 0.55″ pix^{-1} (Benitez et al. 2014). It employs five broadband filters (uJAVA, gSDSS, rSDSS, iSDSS, and zSDSS) and seven narrowband/medium-band filters ($J0378$, $J0395$, $J0410$, $J0430$, $J0515$, $J0660$, and $J0861$) within the optical range. It is essential to note that the S-PLUS iDR4 magnitudes mentioned in this paper refer to the magnitudes calibrated following Almeida-Fernandes et al. (2022).

2.2. Gaia EDR3

Gaia EDR3 (Gaia Collaboration et al. 2021a, 2021b; Riello et al. 2021) provides the most precise photometric data available to date for approximately 1.8 billion stars. The magnitudes in the G, $G_{\rm BP}$, and $G_{\rm RP}$ bands have been uniformly calibrated with accuracy at the millimagnitude level (e.g., Abbott et al. 2021; Niu et al. 2021c). To address magnitude-dependent systematic errors, which are estimated to be around 1% in these bands for Gaia EDR3, Yang et al. (2021) utilized approximately 10,000 Landolt standard stars from Clem & Landolt (2013). In our

[15] http://splus.iag.usp.br

[16] https://noirlab.edu/public/programs/ctio/t80-south-telescope/

study, we adopt the magnitudes of G, $G_{\rm BP}$, and $G_{\rm RP}$ as corrected by Yang et al. (2021) by default.

2.3. Gaia DR3

Gaia DR3 (Gaia Collaboration et al. 2023), based on 34 months of observations, provides ultra-low-resolution ($\lambda/\Delta\lambda \sim 50$) XP spectra for approximately 220 million sources, with the majority having magnitudes $G < 17.65$. The XP spectra cover a wavelength range of 336 to 1020 nm, and have undergone precise internal calibrations (Carrasco et al. 2021; De Angeli et al. 2023), as well as external calibrations (Montegriffo et al. 2023). However, it is crucial to note that Gaia XP spectra are subject to systematic errors that depend on magnitude, color, and extinction, especially at wavelengths below 400 nm (see Montegriffo et al. 2023; Huang et al. 2024). A comprehensive set of corrections, based on reference spectra from CALSPEC and NGSL, have been provided by Huang et al. (2024). In this paper, the term "corrected Gaia XP spectra" refers to the Gaia XP spectra as rectified by Huang et al. (2024).

2.4. LAMOST Data Release 7

The Large Sky Area Multi-object Fiber Spectroscopic Telescope (LAMOST; Cui et al. 2012; Deng et al. 2012; Zhao et al. 2012; Liu et al. 2014) is a quasi-meridian reflecting Schmidt telescope equipped with 4000 fibers and a field of view spanning 20 deg^2. LAMOST's Data Release 7 (DR7; Luo et al. 2015) presents a comprehensive data set comprising 10,640,255 low-resolution spectra, over the full optical wavelength range of 369 to 910 nm, with a spectral resolution of $R \approx 1800$. To derive fundamental stellar parameters, including effective temperature ($T_{\rm eff}$), surface gravity ($\log g$), and metallicity ([Fe/H]), the LAMOST Stellar Parameter Pipeline (LASP; Wu et al. 2011) has been employed. The internal precision typically attained for these parameters is approximately 110 K for $T_{\rm eff}$, 0.2 dex for $\log g$, and 0.1 dex for [Fe/H] $\gtrsim -2.5$ (Luo et al. 2015).

3. Predictions of S-PLUS Magnitudes

In this section, we describe how to obtain the predicted magnitudes for the 12 photometric bands of S-PLUS using the improved XPSP method and SCR method.

3.1. The XPSP Method with Corrected Gaia XP Spectra

The synthetic photometry method (Bessell & Murphy 2012; Gaia Collaboration et al. 2023) involves projecting the SED at the top of the atmosphere of a source onto the transmission curve of the photometric system. Following Xiao et al. (2023c), we compute the synthetic magnitude in the AB system (Oke & Gunn 1983; Fukugita et al. 1996) for each S-PLUS band.

To account for the *u*JAVA band's wavelength range (322–382 nm), slightly bluer than that of the Gaia XP spectra (336 to 1020 nm), we perform numerical extrapolation to extend the Gaia XP spectra. For each source, we obtain a linear function for the Gaia XP spectra's flux density with wavelength through fitting of the Gaia XP spectral data over the range of 336 nm to 382 nm for individual stars. This approach has been proposed and validated in the process of recalibration of J-PLUS photometry, after evaluation of multiple extrapolation methods (Xiao et al. 2023c).

In this study, we select calibration samples satisfying the following constraints: magnitude errors are less than 0.02 mag for the *u*JAVA, *J*0378, and *J*0395 bands, the bluest ones, and less than 0.01 mag for the others. Consequently, we obtain 1,522,862, 1,319,587, 1,002,181, 597,486, 696,915, 2,567,317, 1,325,138, 3,843,548, 3,636,016, 3,984,143, 2,687,153, and 3,391,692 calibration stars in the *u*JAVA, *J*0378, *J*0395, *J*0410, *J*0430, *g*SDSS, *J*0515, *r*SDSS, *J*0660, *i*SDSS, *J*0861, and *z*SDSS bands, respectively. We conduct a count of the standard stars on each image, and present histograms of their distribution in Figure 1.

We emphasize that all the results in this paper are based on the corrected XP spectra of version V1.0 not on the original version V0.1, although the calibration differences between the two versions are negligible (much smaller than 1 mmag in the S-PLUS zero-points).

3.2. The SCR Method with Gaia Photometry and LAMOST Spectra

In principle, the spectroscopy-based SCR method could provide accurate calibrations of zero-points of S-PLUS photometry, just as we have done for the J-PLUS data recently (Xiao et al. 2023c). However, corrections of spatial-related systematics for S-PLUS require a large number of stars targeted by spectroscopic surveys in the southern sky, which is unfortunately not available at present. For this reason, the SCR method is adopted here as an independent way to cross-validate the zero-points derived from the XPSP method.

The SCR method comprises two key techniques: intrinsic-color prediction and reddening correction. The former can be performed based on either spectroscopic or photometric data, while the latter necessitates precise measurement of the reddening coefficients relative to the extinction values. The SCR method typically involves defining the relationship between the intrinsic colors and the physical quantities using a sample of low-extinction stars, which is then applied to the entire sample to obtain predicted magnitudes. A detailed description of the SCR method is as follows.

First, we select calibration samples with the same constraints on photometric recalibration as those of J-PLUS, as in Xiao et al. (2023c), by requiring stars with magnitude errors smaller than 0.02 mag for the *u*JAVA, *J*0378, and *J*0395 bands, and less than 0.01 mag for the remainder; a phot_bp_rp_excess_factor smaller than $1.3 + 0.06 \times (G_{\rm BP} - G_{\rm RP})^2$; a signal-to-noise ratio for the g band of the LAMOST spectra higher than 20; $5500 < T_{\rm eff} < 6500$ K; and [Fe/H] > -1.

Ultimately, we obtain 13,869, 12,714, 10,954, 8814, 9873, 16,301, 14,049, 16,558, 16,522, 16,464, 15,974, and 16,402 calibration stars in the *u*JAVA, *J*0378, *J*0395, *J*0410, *J*0430, *g*SDSS, *J*0515, *r*SDSS, *J*0660, *i*SDSS, *J*0861, and *z*SDSS bands, respectively. Then, we consider 12 colors for the 12 S-PLUS bands when combined with Gaia photometry, denoted as $\boldsymbol{C} = \boldsymbol{G}_{\rm BP/RP} - \boldsymbol{m}_{\rm SPLUS} = (G_{\rm BP} - u{\rm JAVA},\ G_{\rm BP} - J0378,\ G_{\rm BP} - J0395,\ G_{\rm BP} - J0410,\ G_{\rm BP} - J0430,\ G_{\rm BP} - g{\rm SDSS},\ G_{\rm BP} - J0515,\ G_{\rm RP} - r{\rm SDSS},\ G_{\rm RP} - J0660,\ G_{\rm RP} - i{\rm SDSS},\ G_{\rm RP} - J0861$, and $G_{\rm RP} - z{\rm SDSS})$.

To correct for reddening, we adopt the same procedure as that in Xiao & Yuan (2022) and Xiao et al. (2023c). We adopt the values of $E(G_{\rm BP} - G_{\rm RP})$ obtained with the star pair method (Yuan et al. 2013; Zhang & Yuan 2020), and the reddening coefficients with respect to $E(G_{\rm BP} - G_{\rm RP})$ for the 12 colors constructed by H. Yuan et al. (2024, in preparation). Under the assumption that the intrinsic

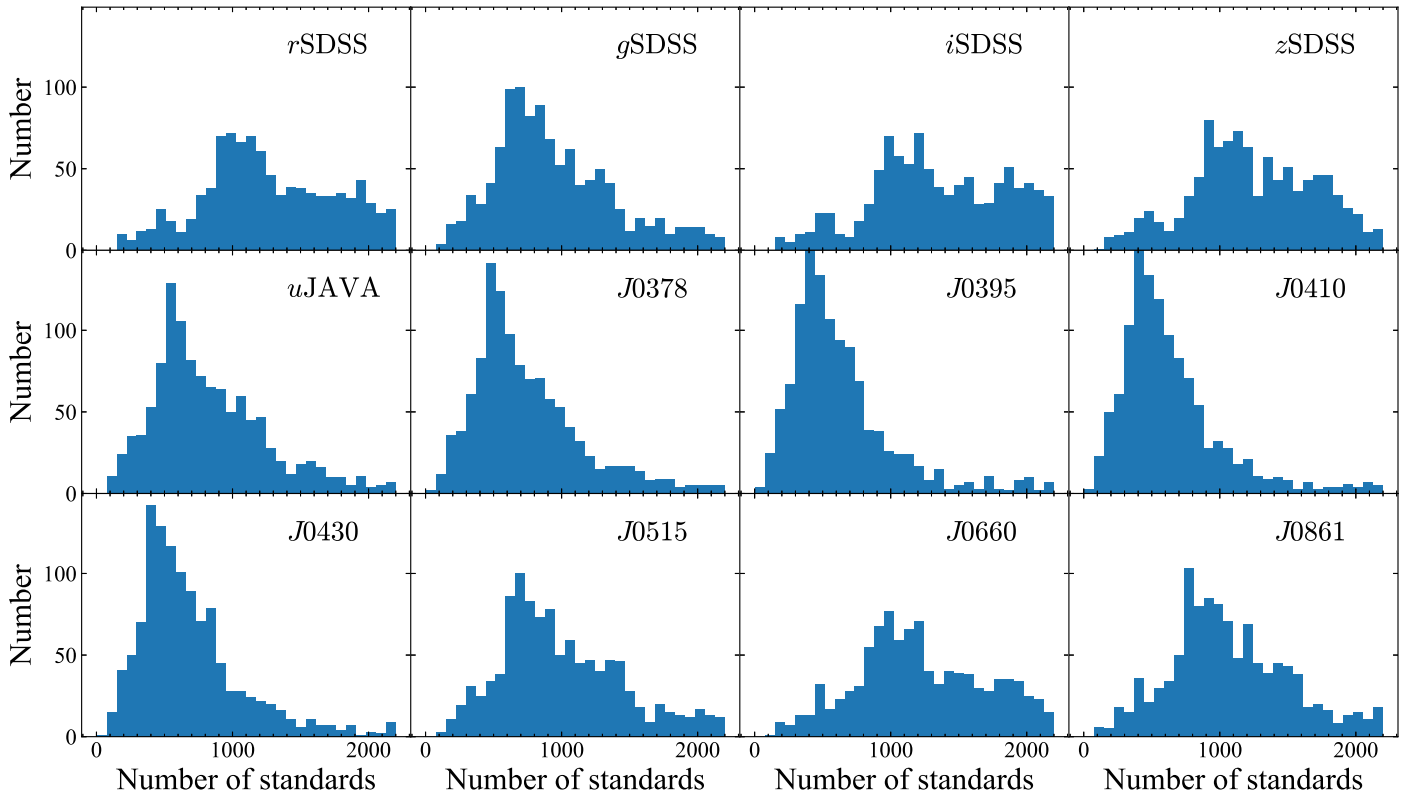

Figure 1. Histograms of the number of standard stars for the XPSP method in each image. The bands are labeled in each panel.

colors are the same for stars with identical stellar atmospheric parameters, the star pair method allows us to derive the intrinsic colors of a reddened star from control pairs or counterparts that share the same atmospheric parameters. In H. Yuan et al. (2024, in preparation), the reddening coefficients for each color are obtained by conducting a linear fit of the calibrated sample's reddening values in relation to $E(G_{\rm BP}-G_{\rm RP})$.

For each color, we fit the intrinsic color as a function of $T_{\rm eff}$ and [Fe/H] using a two-dimensional polynomial. Specifically, we use second-order polynomials for the $G_{\rm RP}-i$, $G_{\rm RP}-J0861$, and $G_{\rm RP}-z$ colors, and third-order polynomials for the other colors. The intrinsic colors (C_0) can then be estimated using the observed colors $\boldsymbol{C}$ minus the product of the reddening coefficients and extinction $E(G_{\rm BP}-G_{\rm RP})$.

The fit results of the intrinsic colors, as a function of $T_{\rm eff}$, [Fe/H], and extinction of $E(G_{\rm BP}-G_{\rm RP})$, are shown in Figure 2, and the corresponding fitting parameters are listed in Table 1. The intrinsic-color fitting residuals are, respectively, 49, 60, 60, 26, 26, 25, 28, 22, 26, 20, 19, and 18 mmag for the $G_{\rm BP}-u$JAVA, $G_{\rm BP}-J0378$, $G_{\rm BP}-J0395$, $G_{\rm BP}-J0410$, $G_{\rm BP}-J0430$, $G_{\rm BP}-g$SDSS, $G_{\rm BP}-J0515$, $G_{\rm RP}-r$SDSS, $G_{\rm RP}-J0660$, $G_{\rm RP}-i$SDSS, $G_{\rm RP}-J0861$, and $G_{\rm RP}-z$SDSS colors, suggesting that S-PLUS magnitudes can be predicted for individual stars with a precision of 20 to 60 mmag using the Gaia and LAMOST data. Furthermore, the fit residuals exhibit no dependence on $T_{\rm eff}$, [Fe/H], and $E(G_{\rm BP}-G_{\rm RP})$.

Having obtained the intrinsic-color fitting functions, we apply them to the calibration stars to obtain the derived magnitudes $m_{\rm SCR}$ for each image using Equation (1):

$$\boldsymbol{m}_{\rm SCR} = \boldsymbol{G}_{\rm BP,RP} - \boldsymbol{C}_0^{\rm mod}(T_{\rm eff},\ [{\rm Fe/H}]) - \boldsymbol{R}\times E(G_{\rm BP}-G_{\rm RP})\,. \quad (1)$$

4. Systematic Errors in S-PLUS iDR4

In this section, we present the process of accurately measuring systematic errors in the S-PLUS photometric data, as well as their origin and correction.

4.1. Dependence on G and $G_{BP}-G_{RP}$

Figure 2 illustrates the relationship between the magnitude offsets predicted by the SCR method and the S-PLUS magnitudes, considering the G magnitude and intrinsic color $(G_{\rm BP}-G_{\rm RP})_0$ of the calibration samples. We observe no discernible dependence with respect to either the G magnitudes or the $(G_{\rm BP}-G_{\rm RP})_0$ color. This indicates that the detector possesses excellent linearity.

We also investigate the differences between the XPSP method magnitude predictions and the S-PLUS magnitudes as functions of the G magnitude and $G_{\rm BP}-G_{\rm RP}$ color. There is a slight dependence on $G_{\rm BP}-G_{\rm RP}$ color, especially in the bluer and redder ranges, in the uJAVA and g bands, as shown in Figure 3. There is no dependence on G magnitude for all the filters. We attribute this effect to measurement errors in the response curve of the S-PLUS iDR4 uJAVA and gSDSS filters, or in the Gaia XP spectra themselves. Certainly, we should not overlook the influence that arises from extrapolating the XP spectra beyond the uJAVA band. Additional details regarding the influence of the response curve on the XPSP method can be found in Xiao et al. (2023c).

For the calibration of the uJAVA and gSDSS bands, we selectively choose stars from specific $G_{\rm BP}-G_{\rm RP}$ ranges of (0.5, 1.2) and (0.5, 1.8), respectively. Moreover, the fraction of stars falling outside the prescribed color range is only 2%–3%.

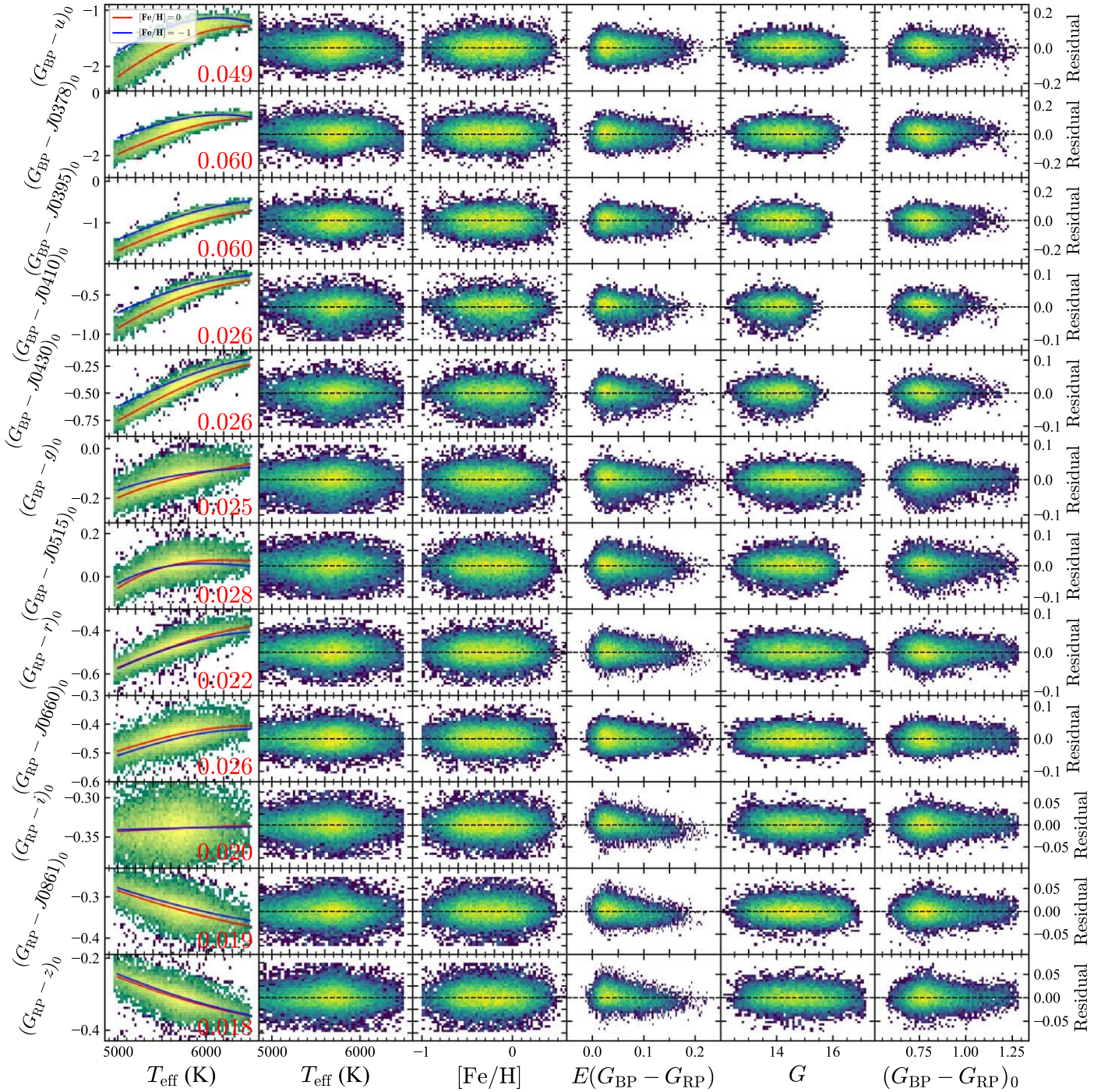

Figure 2. Two-dimensional polynomial fits of the intrinsic colors with respect to $T_{\rm eff}$ and [Fe/H] for the calibration stars in the SCR method. The intrinsic colors include $G_{\rm BP} - u$JAVA, $G_{\rm BP} - J0378$, $G_{\rm BP} - J0395$, $G_{\rm BP} - J0410$, $G_{\rm BP} - J0430$, $G_{\rm BP} - g$SDSS, $G_{\rm BP} - J0515$, $G_{\rm RP} - r$SDSS, $G_{\rm RP} - J0660$, $G_{\rm RP} - i$SDSS, $G_{\rm RP} - J0861$, and $G_{\rm RP} - z$SDSS. The fit results after 3σ clipping are shown in the first column of panels, with the red and blue curves representing results for [Fe/H] = 0 and [Fe/H] = −1, respectively. The fit residuals are labeled in red. In the second to sixth columns of panels, the residuals are plotted against $T_{\rm eff}$, [Fe/H], extinction of $E(G_{\rm BP} - G_{\rm RP})$, G magnitude, and $(G_{\rm BP} - G_{\rm RP})_0$ color, respectively. Zero residuals are denoted by black dashed lines.

4.2. Spatial Variations

We consider the spatial distribution of the difference between zero-points for the XPSP method and the S-PLUS aperture magnitudes for the main survey, as shown in Figure 4. The results for the MCs with aperture photometry, the main survey with PSF photometry, the MCs with PSF photometry, and the disk survey with PSF photometry are plotted in Figures A1, A2, A3, and A4, respectively, in the Appendix. The difference in zero-points between the XPSP method and the S-PLUS magnitudes is computed as the median value of the difference between the XPSP-predicted magnitudes and the S-PLUS magnitudes on each image. We observe strong spatial variations in the difference of the zero-points, caused by calibration errors in S-PLUS, which are more pronounced in

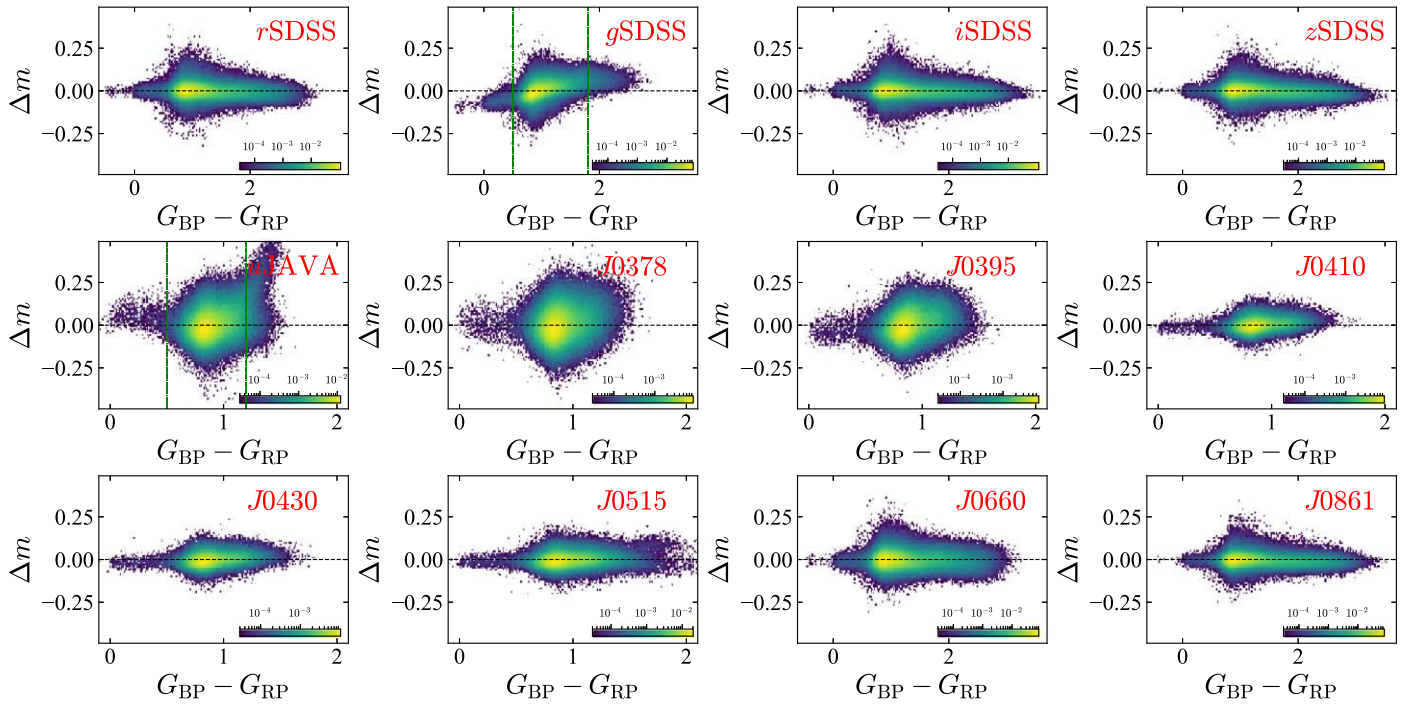

Figure 3. Magnitude offsets between the XPSP-predicted magnitudes and the S-PLUS magnitudes, as a function of $G_{BP} - G_{RP}$ color, for all 12 bands. The colors represent the density of points, and the bands are indicated in each panel. Zero residuals and two color cuts are denoted by black and green dashed lines, respectively. Color bars are plotted in the lower-right corner of each panel.

Table 1
Coefficients Used to Obtain Intrinsic Colors as Functions of $T_{\rm eff}$ and [Fe/H] in the 12 Bands

Intrinsic Color	a_0	a_1	a_2	a_3	a_4	a_5	a_6	a_7	a_8	a_9
$(G_{BP} - u\mathrm{JAVA})_0$	−6.140e11	+0.006	+5.692e8	+1.269e5	+6.605e7	−1.901e1	−3.964e4	−8.742e4	−0.028	−6.650
$(G_{RP} - J0378)_0$	−1.392e10	+0.023	+9.537e8	−1.723e5	+1.984e6	+7.471e5	−8.069e4	−8.177e3	+1.026	+6.731
$(G_{RP} - J0395)_0$	−2.697e11	+0.075	−1.265e8	−1.121e5	+2.235e7	+1.053e1	+0.0002	+7.561e4	−0.746	−7.669
$(G_{RP} - J0410)_0$	−1.376e12	−0.002	−3.555e8	+6.523e5	−1.614e7	−4.446e1	+5.634e4	+2.398e3	−2.244	−8.709
$(G_{RP} - J0430)_0$	−3.228e11	+0.022	−9.292e9	−8.655e6	+4.584e7	+5.971e2	+1.536e4	−1.705e3	−0.676	+0.345
$(G_{BP} - g\mathrm{SDSS})_0$	+1.745e11	+0.004	+2.991e9	−4.360e6	−3.311e7	+1.609e2	−9.492e6	+2.158e3	−0.067	−4.891
$(G_{RP} - J0515)_0$	+3.762e11	+0.007	−8.821e9	+2.966e6	−7.439e7	−2.790e2	+1.346e4	+4.886e3	−0.493	−10.589
$(G_{RP} - r\mathrm{SDSS})_0$	−9.563e12	+0.018	+1.687e8	−1.396e5	+1.278e7	+9.315e2	−0.0002	−3.890e4	+0.555	−0.624
$(G_{RP} - J0660)_0$	−8.887e12	+0.015	+1.730e9	−1.054e5	+1.206e7	+7.299e2	−3.287e5	−4.427e4	+0.142	−0.185
$(G_{BP} - i\mathrm{SDSS})_0$	⋯	⋯	⋯	⋯	−1.038e9	−3.942e3	+2.666e6	+1.701e5	−0.019	−0.402
$(G_{BP} - J0861)_0$	⋯	⋯	⋯	⋯	+1.110e8	−3.099e4	−4.378e6	−1.853e4	+0.015	+0.365
$(G_{RP} - z\mathrm{SDSS})_0$	⋯	⋯	⋯	⋯	+1.630e8	−1.335e3	+3.958e6	−0.853e4	−0.029	+0.639

Notes. The notation ei represents $\times 10^{-i}$. $C_0^{\rm mod} = a_0 \cdot x^3 + a_1 \cdot y^3 + a_2 \cdot x^2 \cdot y + a_3 \cdot x \cdot y^2 + a_4 \cdot x^2 + a_5 \cdot y^2 + a_6 \cdot x \cdot y + a_7 \cdot x + a_8 \cdot y + a_9$, where x is $T_{\rm eff}$ and y is [Fe/H].

the blue filters. Simultaneously, we notice spatial correlations in the differences in zero-points between the different S-PLUS bands. The reasons for this are discussed in detail in Section 4.3.

To quantitatively estimate calibration errors in the S-PLUS photometry, we consider histograms of the difference in zero-points between the XPSP method and the S-PLUS magnitudes, as shown in Figure 5. By fitting a Gaussian distribution, we estimate the standard deviations for each band. Here, to better illustrate the effect, we forcibly set the overall zero-point difference to zero. During the recalibration process, we calibrate the zero-point of the S-PLUS magnitudes to the XPSP method. These values indicate the internal precision of S-PLUS iDR4, as mentioned in Almeida-Fernandes et al. (2022), and listed in Table 2.

4.3. Origin and Correction of Systematic Errors

In order to trace the origin of the systematic errors in the S-PLUS photometry, we plot correlations between the zero-point offsets for each band pair in Figure 6, along with their corresponding correlation coefficients when the correlation coefficients are greater than 0.7. We find a strong correlation between photometric bands with similar central wavelengths (e.g., ΔiSDSS versus ΔzSDSS): the data points are distributed closely along the one-to-one line. This phenomenon is predominantly driven by systematic errors in the reference

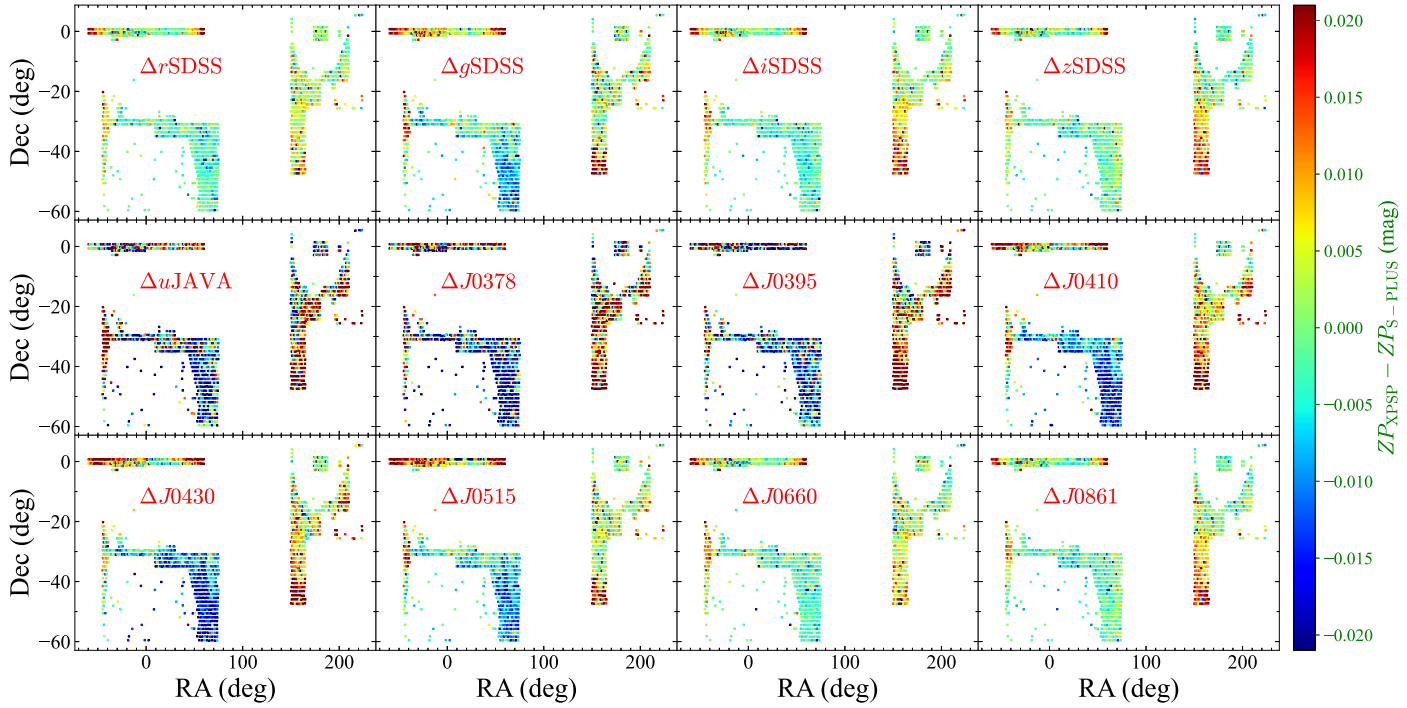

Figure 4. Spatial variations of the difference between the XPSP zero-points and the S-PLUS zero-points in each image of the main survey, using PStotal photometry from S-PLUS. The bands are marked in each panel in red, and the color bar indicating the differences is shown on the right.

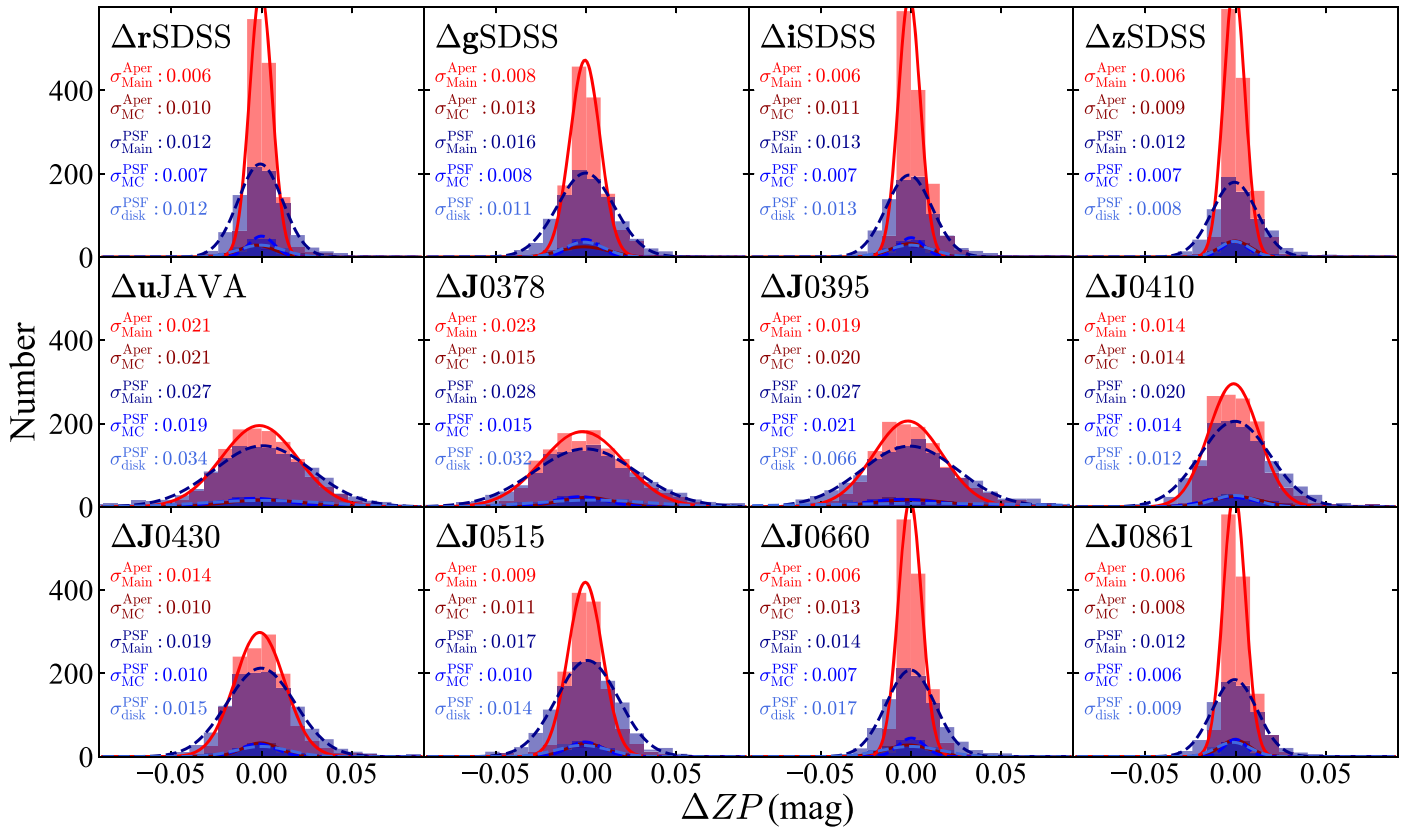

Figure 5. Histograms of the residuals in the zero-points between the XPSP magnitudes, along with the S-PLUS magnitudes. The results shown are for the main survey with PStotal photometry (light red), the MCs with PStotal photometry (dark red), the main survey with PSF photometry (purple), the MCs with PSF photometry (blue), and the disk region with PSF photometry (light blue). The bands are labeled in the top-left corner of each panel. Gaussian fitting results are plotted with the same colors, using solid and dashed curves for PStotal photometry and PSF photometry, respectively. The sigma values are labeled on the left side of each panel with the same colors.

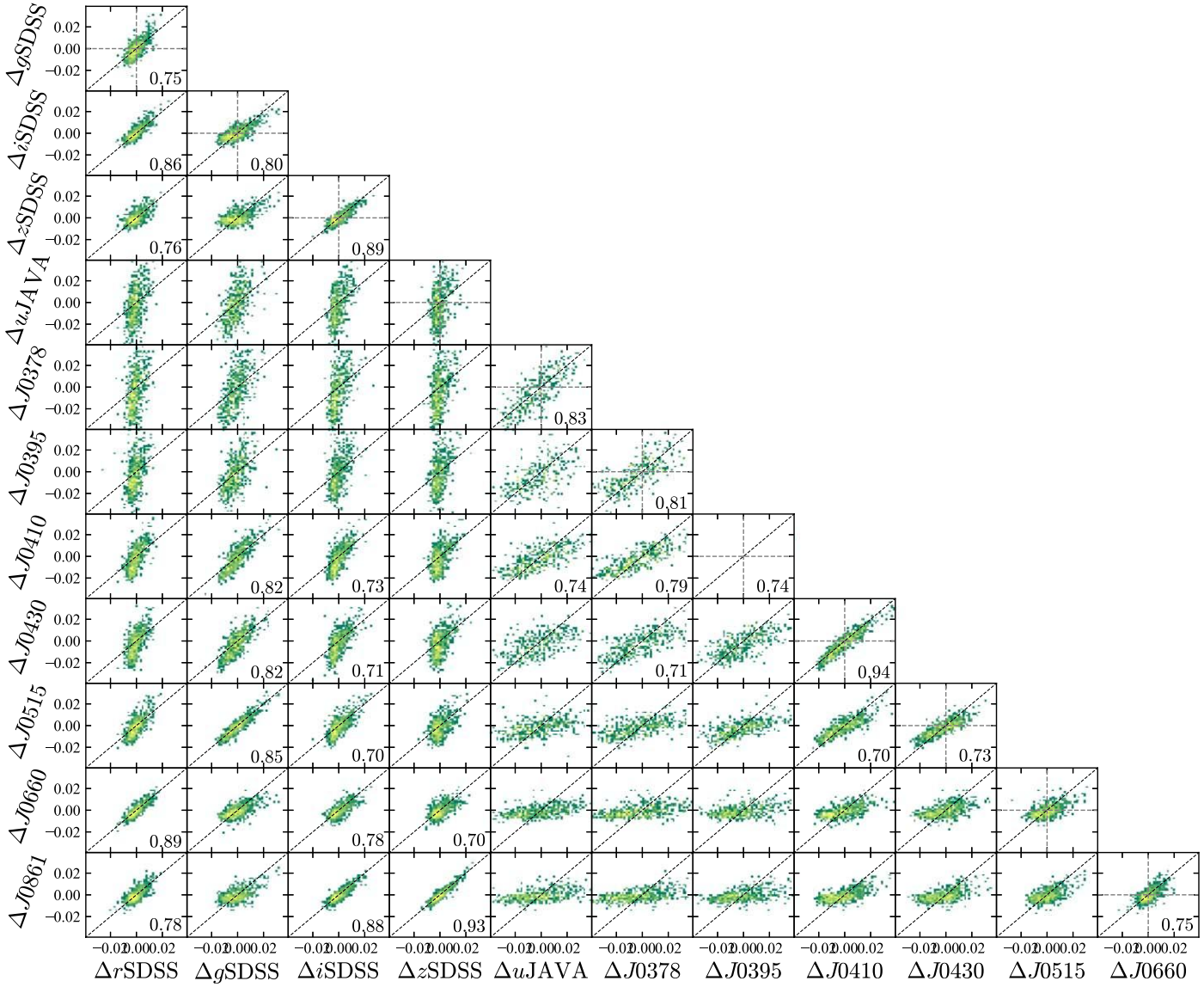

Figure 6. Correlation plots between the zero-point offsets. The correlation coefficients are shown when they have values greater than 0.7. The colors in each panel indicate the number density of stars, and the dashed black lines represent the one-to-one line.

photometric data in the respective bands. For example, the systematic errors in the S-PLUS i and z bands are predominantly influenced by the systematic errors in the Pan-STARRS and SDSS photometric data (e.g., the color and photometric recalibration of SDSS Stripe 82 can be found in Yuan et al. 2015 and Huang & Yuan 2022, while the photometric recalibration of PS1 can be found in Xiao & Yuan 2022 and Xiao et al. 2023b).

To correct the above systematic errors, we perform a smoothed interpolation algorithm with a linear kernel for each image. The magnitude correction of a certain star in the field of view is obtained by taking the magnitude offsets of the adjacent 20 calibration stars. The corrected magnitude $m^{\rm corr}$ can be computed as

$$m^{\rm corr} = m^{\rm obs} + \Delta m(\text{R.A.}, \text{decl.}) \,, \tag{2}$$

where $m^{\rm obs}$ is the observed magnitude from S-PLUS iDR4, and Δm(R.A., decl.) is the position-dependent magnitude offset. The recalibrated S-PLUS data will be released as a value-added catalog of S-PLUS Data Release 4 by S-PLUS Cloud.[17]

5. Discussion

This section applies to the S-PLUS iDR4 main survey data, using it as an illustration for discussion.

5.1. Final Accuracies

The consistency between the photometry from the two methods is adopted as a measure of accuracy, which provides a reasonable approximation in the absence of a "reference truth" to compare with.

Figure 7 shows a comparison of zero-points between the XPSP method and the SCR method for all 12 S-PLUS filters. The differences between these zero-points are computed as the median value of the difference between the XPSP- and SCR-

[17] https://splus.cloud/

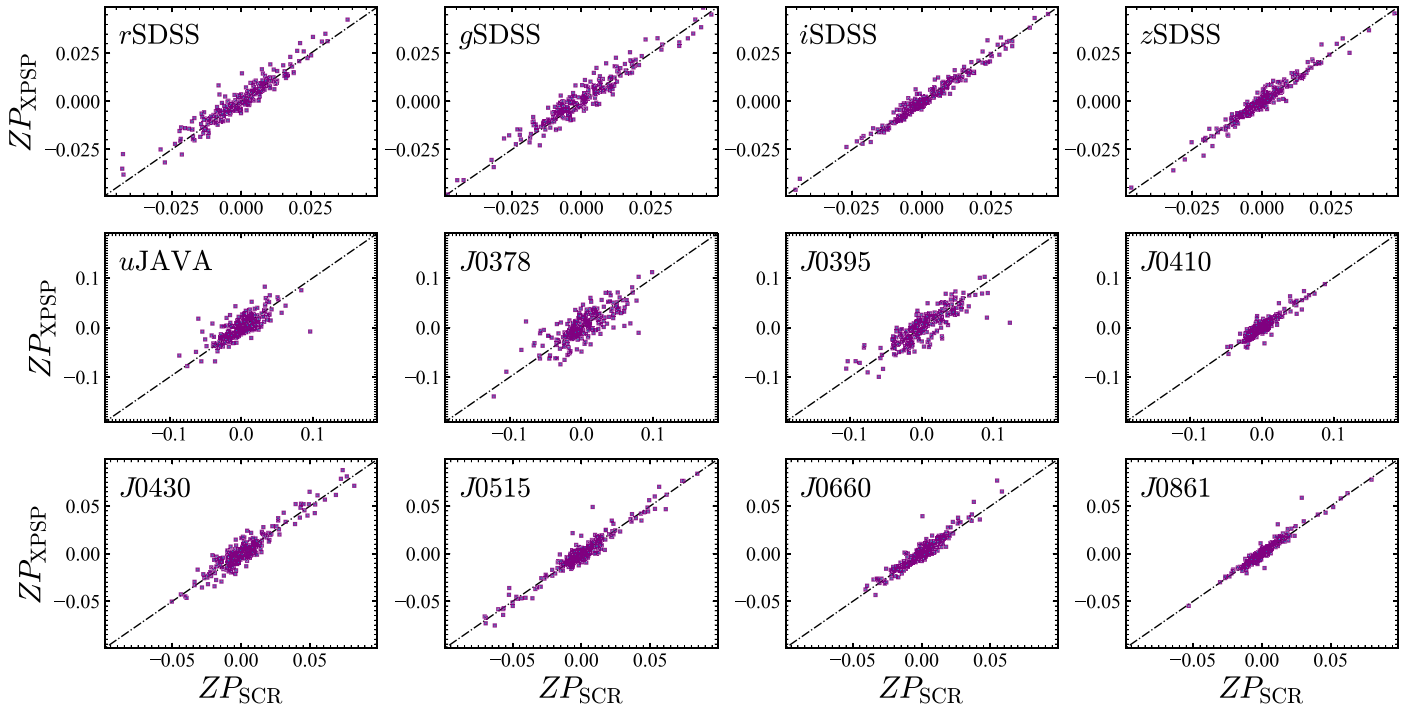

Figure 7. Comparison of the zero-points for each of the two methods based on stars common to both the XPSP and SCR methods' samples for all 12 bands. The dashed black lines represent the one-to-one line.

predicted magnitudes for each image. From inspection, all the points are consistently distributed along the one-to-one line for each band.

To quantitatively estimate the final accuracies of the recalibration in this work, we present the difference in zero-points between the XPSP method and SCR method, as a function of star number, in Figure 8. Notably, the standard deviations start at higher values, then decrease and converge to stable values as the number of stars increases. The convergence value represents the recalibrated accuracy using the XPSP method, which is 1–6 mmag for each of the 12 bands. For each of 12 bands, the final accuracies of the S-PLUS iDR4 data are similar in the main survey, the MCs, and the disk survey, as listed in the last column of Table 2.

5.2. External Check by White Dwarf Loci

We provide an independent check of the recalibration using a white dwarf (WD) locus, known for its stability and uniformity at different spatial locations.

To accomplish this, we crossmatch the WD catalog constructed by Gaia Collaboration et al. (2023) from Gaia EDR3 with the S-PLUS iDR4 catalog. We impose the criterion Galactic latitude $|b| > 20°$ for the selected WDs to ensure that the best photometry is used. Specifically, we focus on the behavior of the *u*JAVA band, as the photometric systematics in the other bands are relatively small and difficult to examine with the WD locus. Additionally, we require that the photometric uncertainties of the *u*JAVA band from S-PLUS iDR4 be smaller than 0.01 mag. After the crossmatch, we retain 100 WDs with good photometric quality. The stellar loci, $G - u$JAVA versus $G_{\rm BP} - G_{\rm RP}$, of the selected WDs are shown in Figure 9. From inspection, the WD locus from the S-PLUS photometry for the *u*JAVA band with R.A. $< 90°$ and decl. $< -40°$ (red dots) significantly deviates from that with R.A. $> 180°$ and decl. $> -30°$ (black dots). However, the WD loci for different positions provided by our recalibrated S-PLUS iDR4 photometry exhibit remarkable consistency, demonstrating the efficacy of both the XPSP method and SCR method in calibrating the photometric zero-points.

Table 2
Internal Precision of the Photometric Calibration for the 12 S-PLUS Bands

Filter	$\rm Main_{Ap}$	$\rm Main_{PSF}$	$\rm MCs_{Ap}$	$\rm MCs_{PSF}$	$\rm Disk_{PSF}$	Final Accuracy
			(mmag)			
*g*SDSS	6	12	10	7	12	0.8
*r*SDSS	8	16	13	8	11	1.6
*i*SDSS	6	13	11	7	13	1.0
*z*SDSS	6	12	9	7	8	0.6
*u*JAVA	21	27	21	19	34	6.1
*J*0378	23	28	15	15	32	5.7
*J*0395	19	27	20	21	66	4.1
*J*0410	14	20	14	14	12	1.9
*J*0430	14	19	10	10	15	2.8
*J*0515	9	17	11	10	14	1.1
*J*0660	6	14	13	7	17	2.6
*J*0861	6	12	8	6	9	0.9

5.3. Residuals of the Flat-field Correction

S-PLUS utilizes the sky flat-fielding technique (Mendes de Oliveira et al. 2019) for this correction. However, Almeida-Fernandes et al. (2022) found spatial structures in the residuals of the flat-field correction in the Galactic (X, Y) plane, and corrected them with numerical interpolation. In this study, we further investigate whether there are any related systematic errors in this plane before and after recalibration of the S-PLUS photometry. Specifically, we focus on the *g*SDSS, *J*0515, and

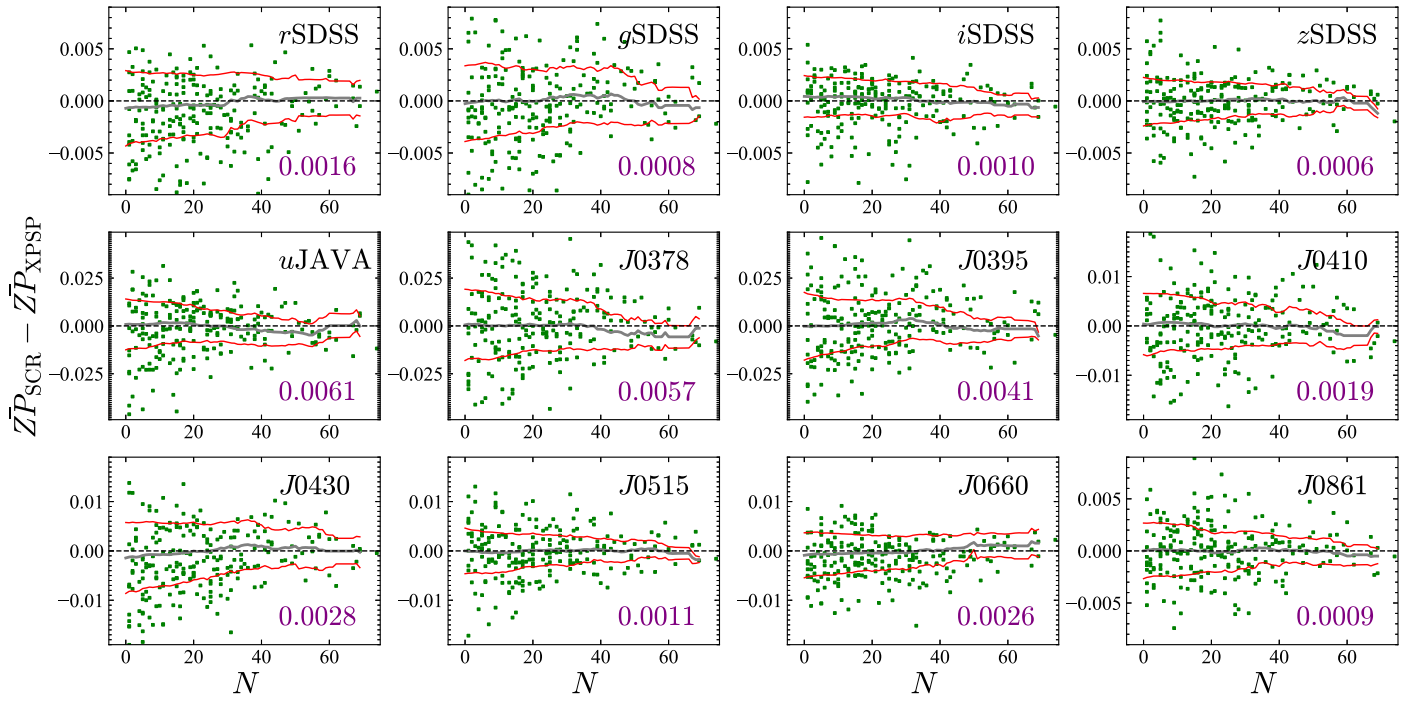

Figure 8. Comparison of the zero-points for each of the two methods based on stars common to both the XPSP and SCR methods' samples for all 12 bands, as a function of star number (denoted as N) in each image. The bands are marked in each panel. The green points show the difference of the zero-points, and their median values and standard deviations are estimated using Gaussian fitting with a running width of 15 stars and a running step of 1 star, and are indicated by the gray and red curves, respectively. The median value of the standard deviations, for N ranging from 60 to 70, is labeled in each panel. The dashed black lines represent the zero-residual line. The distribution of zero-point differences is not symmetric about zero at intermediate and/or large N, and is primarily due to the limited common fields covered by both LAMOST (a northern-sky survey) and S-PLUS (a southern-sky survey). But the decreasing trend of scatter along N is clearly seen in all bands.

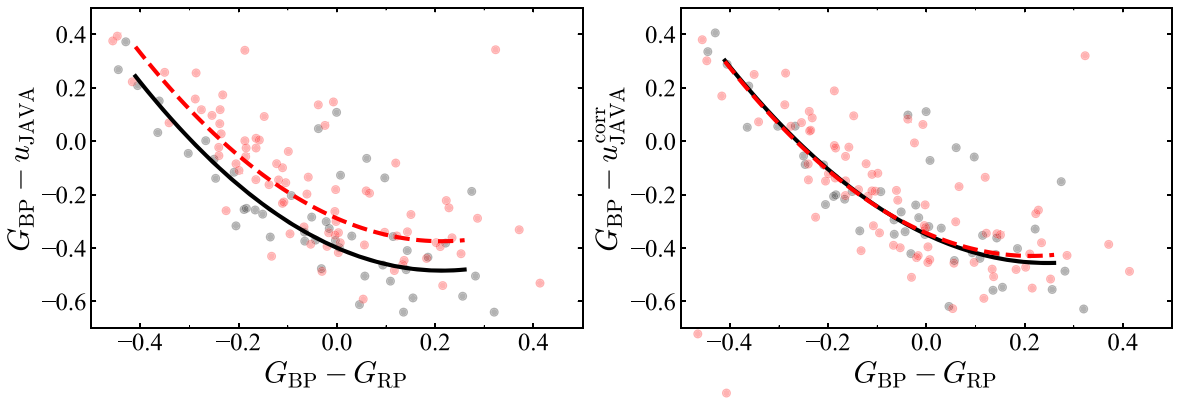

Figure 9. The WD loci $G - u$JAVA vs. $G_{\rm BP} - G_{\rm RP}$ before (left panel) and after (right) recalibration in the uJAVA band. The red and black points represent the R.A. $< 90°$ and decl. $< -40°$ region and the R.A. $> 180°$ and decl. $> -30°$ region, respectively. The red dashed curve and the black curve correspond to the quadratic polynomial fitting results for the red and black dots, respectively.

J0861 bands as examples. We select three images with IDs of iDR4_3_HYDRA−0161, iDR4_3_HYDRA−0152, and iDR4_3_HYDRA−0145 for this investigation, because they contain the largest number of reference stars, approximately 10,000 to 20,000 stars. The images can be retrieved from the S-PLUS cloud.[17]

From Figure 10, we observe distinct spatial structures in the stellar flat fields, with variations larger than 0.01 mag. Notably, the structures for each image differ from one another. For instance, the top panel (iDR4_3_HYDRA−0161) exhibits a trend of larger values in the center and smaller values at the edges. Conversely, the middle panel (iDR4_3_HYDRA−0152) displays a trend of smaller values in the center and smaller values at the edges. Lastly, the bottom panel (iDR4_3_HYDRA−0145) shows a trend of smaller values on the left side and larger values on the right side. However, despite these variations, the structures are consistent for different wavelength observations of each image. These structures, which may occur as residual artifacts following the sky flat-field correction, can be effectively corrected during the recalibration process, as shown in Figure 11.

6. Conclusions

In this paper, we present a recalibration of S-PLUS photometry using millions of standards constructed by the XPSP method with corrected Gaia XP spectra. Additionally, we employ the SCR method with corrected Gaia EDR3

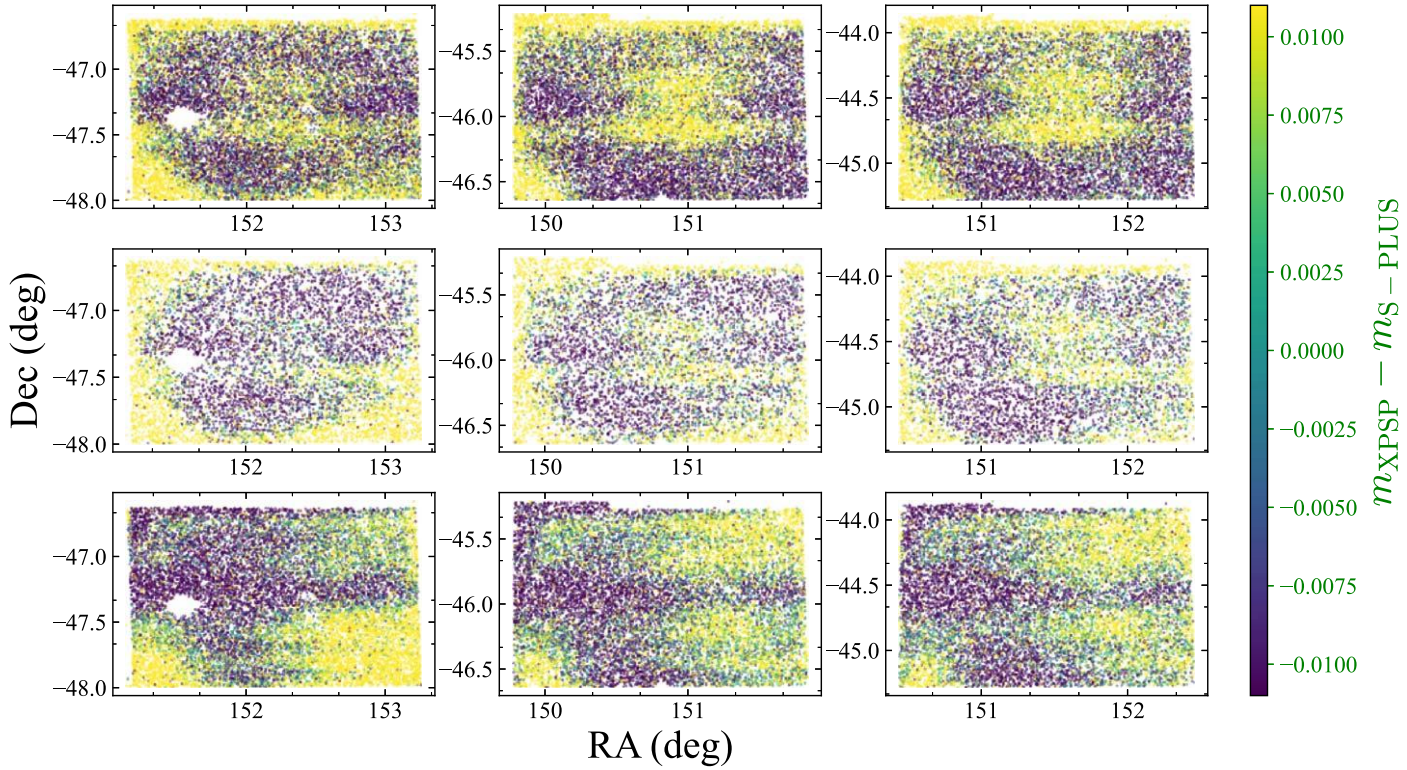

Figure 10. An example showing the spatial distribution over the CCD of the difference between the XPSP method and the S-PLUS magnitudes. From left to right, the results are shown for the *g*SDSS, *J*0515, and *J*0861 bands. From top to bottom, three different observations are shown with tile_id of HYDRA−0161, HYDRA −0152, and HYDRA−0145. A color bar is shown on the right.

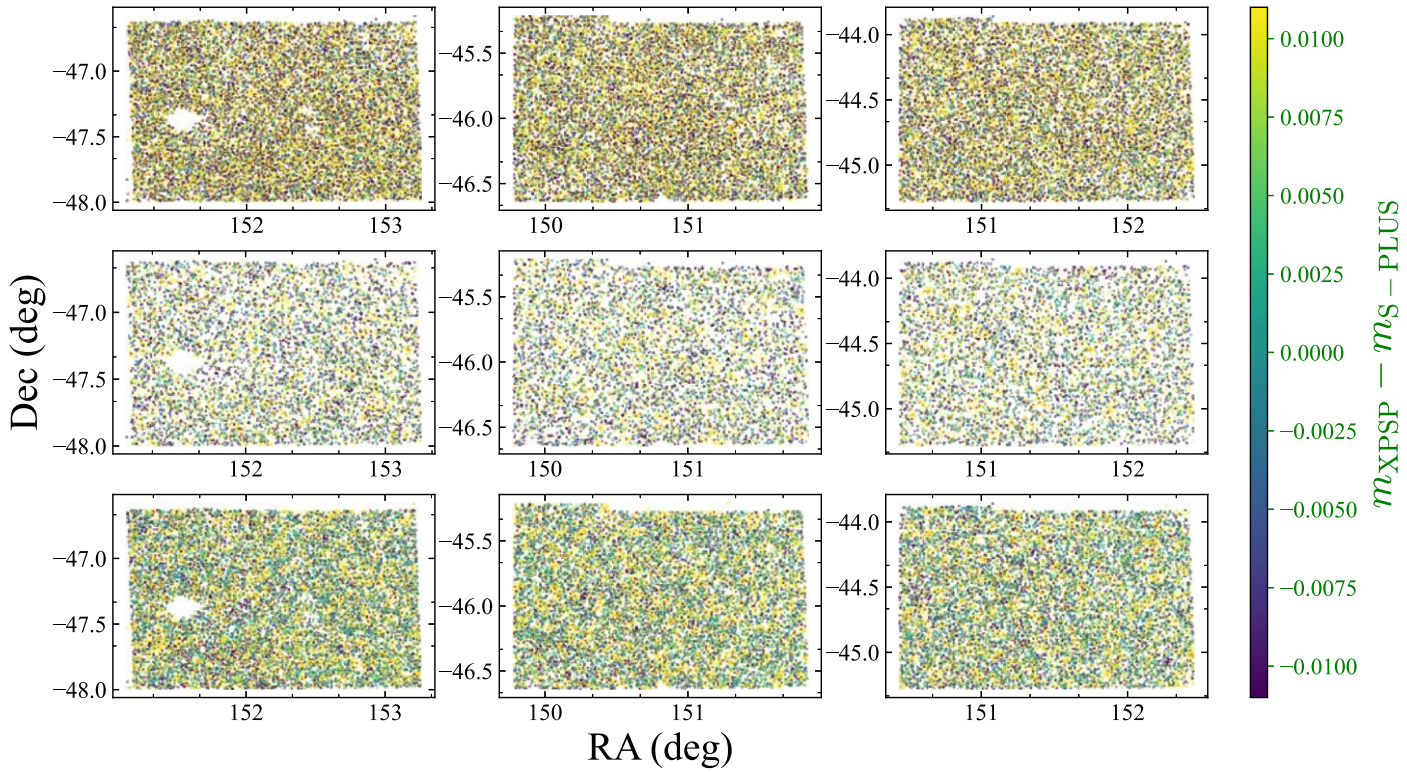

Figure 11. Same as Figure 10, but for the results after recalibration.

photometric data and spectroscopic data from LAMOST DR7 to construct a sample of about 200 FGK dwarf standard stars per band, providing an independent validation.

During the comparison of zero-points between the XPSP method and S-PLUS photometric data, significant spatial variations of the zero-point offsets are identified, reaching up

to 14–23 mmag for the blue filters (*u*JAVA, *J*0378, *J*0395, *J*0410, and *J*0430), 6–8 mmag for the SDSS-like filters (*g*SDSS, *r*SDSS, *i*SDSS, and *z*SDSS), and 6–9 mmag for the redder filters (*J*0515, *J*0660, and *J*0861).

Similarly, when comparing the zero-points between the XPSP and SCR methods, we find minor differences in zero-point offsets, approximately 3–6 mmag for the blue filters, 1–2 mmag for the SDSS-like filters, and 1–3 mmag for the redder filters. These results show that the recalibration achieves an accuracy of approximately 1 to 6 mmag, when using the XPSP method in this work.

To validate our recalibration results, we examine the color locus of WDs, and as expected, the distribution of WDs on the color–color diagram appears more compact after recalibration than before. Additionally, we discuss the minor systematic errors related to CCD position, and identify almost no remaining residuals in the flat-field correction of the S-PLUS photometry. The corrected S-PLUS iDR4 photometric data will provide a solid data foundation for conducting scientific research that relies on high calibration precision.

Overall, our results underscore the effectiveness of the improved XPSP method and the SCR method in improving calibration precision for wide-field surveys, when combined with spectroscopic data from spectroscopic surveys (LAMOST, etc.), Gaia photometry, and XP spectra. We propose that future releases of S-PLUS photometry should incorporate the XPSP method paired with the SCR method in their calibration process.

Acknowledgments

This work is supported by the National Key Basic R&D Program of China via 2023YFA1608300; the China Postdoctoral Science Foundation of 2023M743447; the National Natural Science Foundation of China through the projects NSFC 12222301, 12173007, and 11603002; the National Key Basic R&D Program of China via 2019YFA0405503; and Beijing Normal University grant No. 310232102. We acknowledge science research grants from the China Manned Space Project No. CMS-CSST-2021-A08 and CMS-CSST-2021-A09. T.C.B. acknowledges partial support from grant PHY 14-30152 of the Physics Frontier Center/JINA Center for the Evolution of the Elements (JINA-CEE) and from OISE-1927130 of the International Research Network for Nuclear Astrophysics (IReNA), awarded by the US National Science Foundation. G.L. acknowledges funding from FAPESP (procs. 2021/10429-0 and 2022/07301-5). F.A.-F. acknowledges funding for this work from FAPESP grant 2018/20977-2. S-PLUS as a whole acknowledges grant 2019/26492-3 from FAPESP.

The S-PLUS project, including the T80-South robotic telescope and the S-PLUS scientific survey, was founded as a partnership between the Fundação de Amparo à Pesquisa do Estado de São Paulo (FAPESP), the Observatório Nacional, the Federal University of Sergipe (UFS), and the Federal University of Santa Catarina (UFSC), with important financial and practical contributions from other collaborating institutes in Brazil, Chile (Universidad de La Serena), and Spain (Centro de Estudios de Física del Cosmos de Aragón, CEFCA). We further acknowledge financial support from the São Paulo Research Foundation (FAPESP), the Fundação de Amparo à Pesquisa do Estado do RS (FAPERGS), the Brazilian National Research Council (CNPq), the Coordination for the Improvement of Higher Education Personnel (CAPES), the Carlos Chagas Filho Rio de Janeiro State Research Foundation (FAPERJ), and the Brazilian Innovation Agency (FINEP). Members of the S-PLUS collaboration are grateful for the contributions of the CTIO staff to the construction, commissioning, and maintenance of the T80-South telescope and camera.

This work has made use of data from the European Space Agency (ESA) mission Gaia (https://www.cosmos.esa.int/gaia), processed by the Gaia Data Processing and Analysis Consortium (DPAC; https://www.cosmos.esa.int/web/gaia/dpac/consortium). Funding for the DPAC has been provided by national institutions, in particular the institutions participating in the Gaia Multilateral Agreement. Guoshoujing Telescope (the Large Sky Area Multi-object Fiber Spectroscopic Telescope, LAMOST) is a national major scientific project built by the Chinese Academy of Sciences. Funding for the project has been provided by the National Development and Reform Commission. LAMOST is operated and managed by the National Astronomical Observatories, Chinese Academy of Sciences.

Appendix

The spatial distributions of the difference between zero-points for the XPSP method and the S-PLUS aperture photometry for the MCs, the PSF photometry for the main survey, the PSF photometry for the MCs, and the PSF photometry for the disk survey are shown in Figures A1, A2, A3, and A4, respectively. The zero-point offsets between the XPSP method and the S-PLUS photometry for each band are mainly caused by systematic errors in the calibration of the S-PLUS photometry.

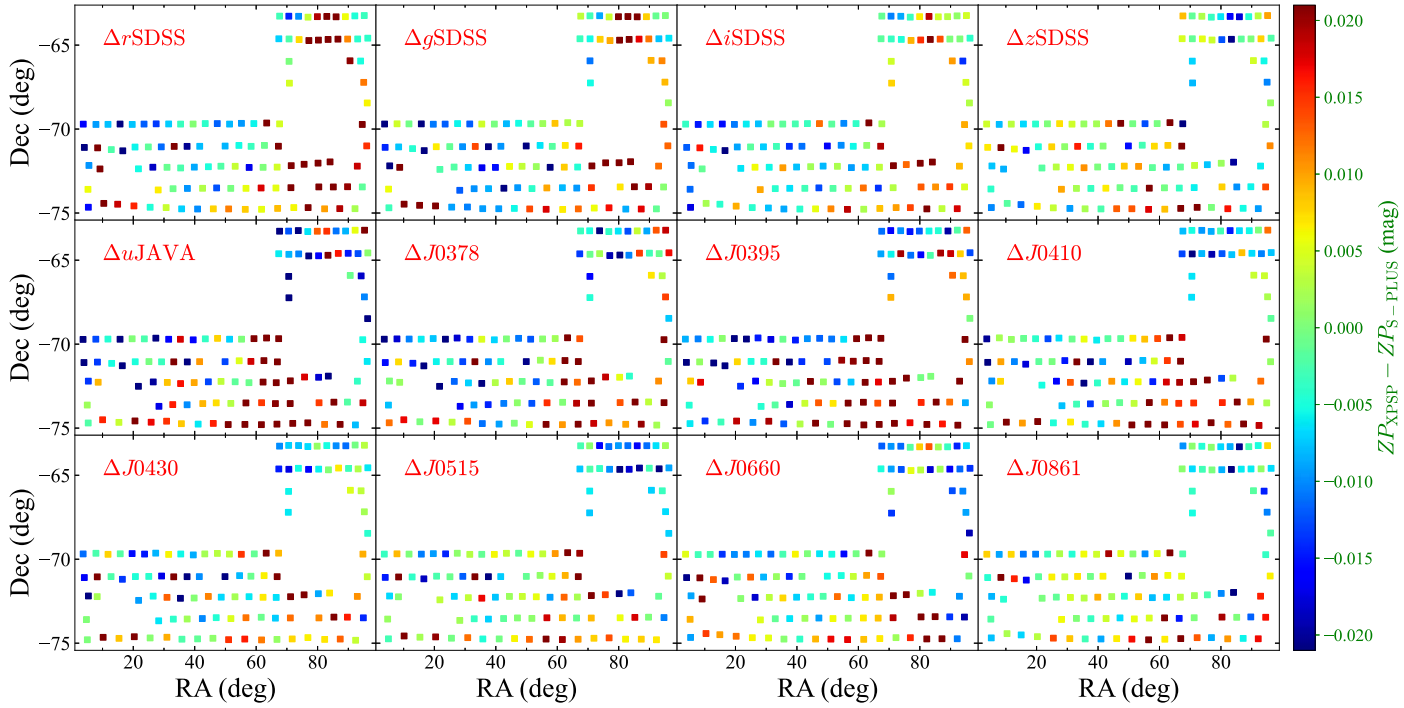

Figure A1. Same as Figure 4, but for the MCs with PStotal photometry.

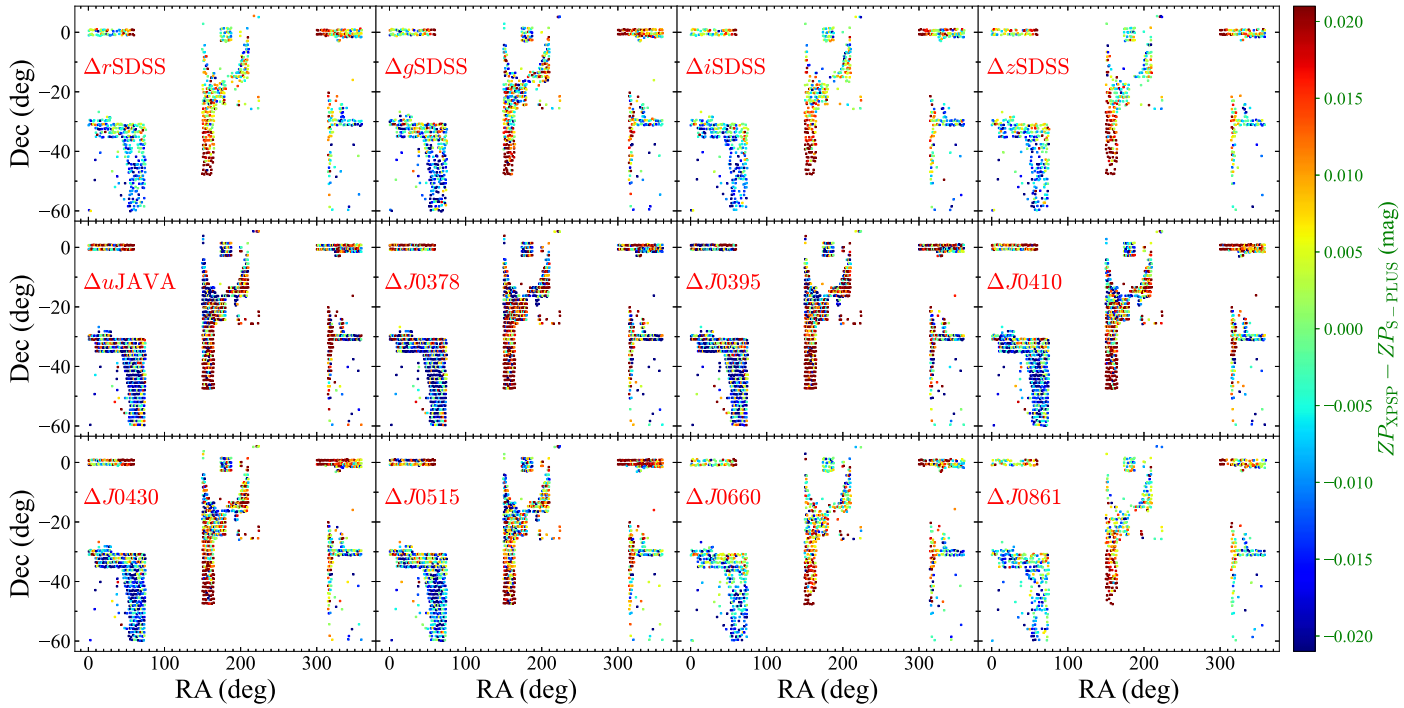

Figure A2. Same as Figure 4, but for the main survey with PSF photometry.

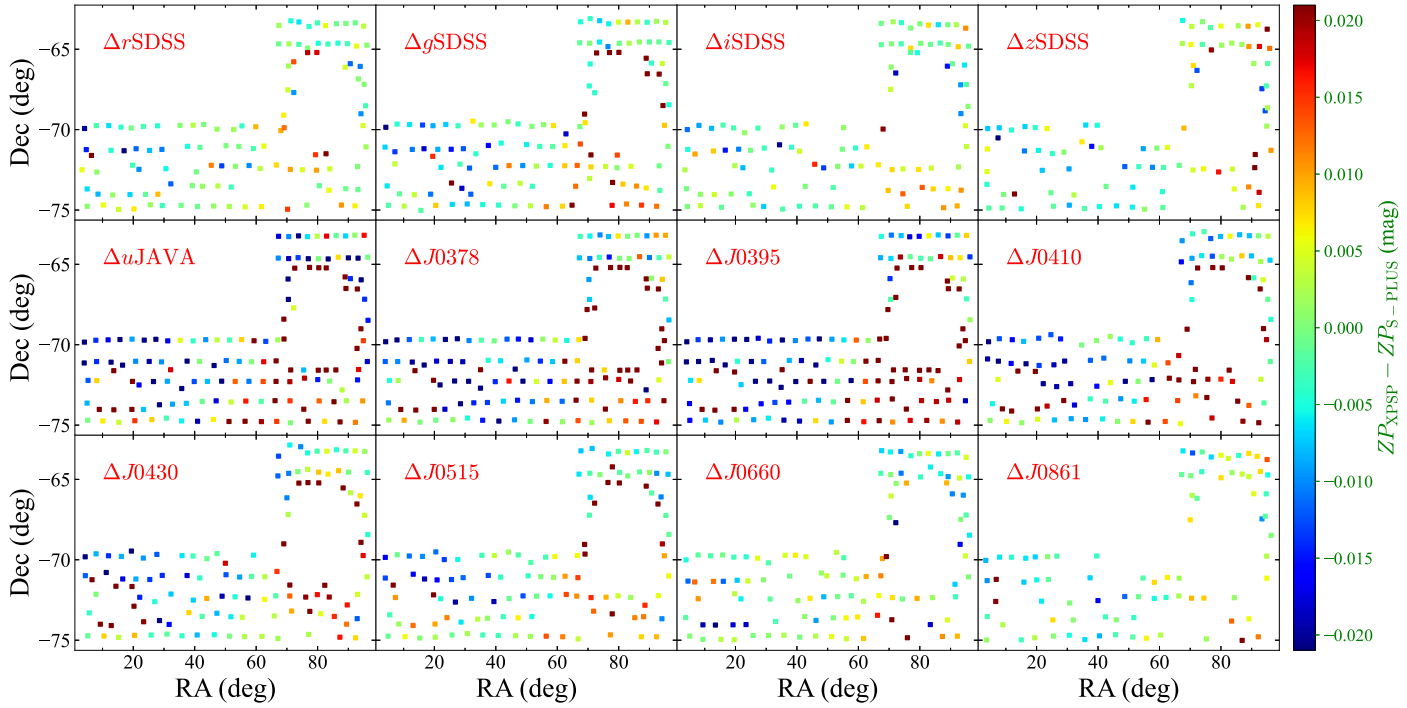

Figure A3. Same as Figure 4, but for the MCs with PSF photometry.

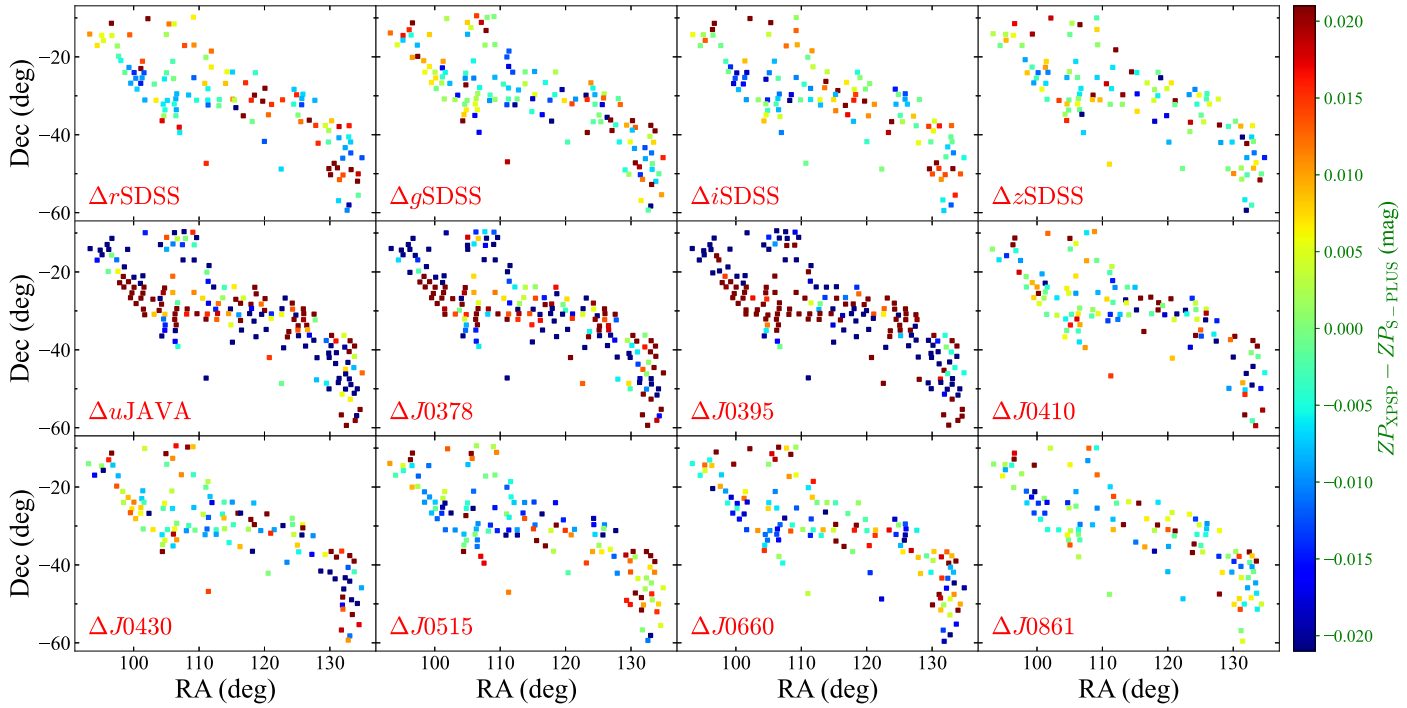

Figure A4. Same as Figure 4, but for the disk survey with PSF photometry.

ORCID iDs

Kai Xiao https://orcid.org/0000-0001-8424-1079
Haibo Yuan https://orcid.org/0000-0003-2471-2363
Timothy C. Beers https://orcid.org/0000-0003-4573-6233
Bowen Huang https://orcid.org/0000-0002-1259-0517
Shuai Xu https://orcid.org/0000-0003-3535-504X
Lin Yang https://orcid.org/0000-0002-9824-0461
Felipe Almeida-Fernandes https://orcid.org/0000-0002-8048-8717
Hélio D. Perottoni https://orcid.org/0000-0002-0537-4146
Guilherme Limberg https://orcid.org/0000-0002-9269-8287
William Schoenell https://orcid.org/0000-0002-4064-7234
Tiago Ribeiro https://orcid.org/0000-0002-0138-1365
Antonio Kanaan https://orcid.org/0009-0007-8005-4541
Natanael Gomes de Oliveira https://orcid.org/0009-0005-1424-6604

References

Abbott, T. M. C., Adamów, M., Aguena, M., et al. 2021, ApJS, 255, 20
Almeida-Fernandes, F., SamPedro, L., Herpich, F. R., et al. 2022, MNRAS, 511, 4590
Benitez, N., Dupke, R., Moles, M., et al. 2014, arXiv:1403.5237
Bessell, M., & Murphy, S. 2012, PASP, 124, 140
Bohlin, R. C., Gordon, K. D., & Tremblay, P.-E. 2014, PASP, 126, 711
Bohlin, R. C., & Lockwood, S. 2022, Instrument Science Report, STScI, STIS 2022-7
Burke, D. L., Rykoff, E. S., Allam, S., et al. 2018, AJ, 155, 41
Carrasco, J. M., Weiler, M., Jordi, C., et al. 2021, A&A, 652, A86
Clem, J. L., & Landolt, A. U. 2013, AJ, 146, 88
Cui, X.-Q., Zhao, Y.-H., Chu, Y.-Q., et al. 2012, RAA, 12, 1197
De Angeli, F., Weiler, M., Montegriffo, P., et al. 2023, A&A, 674, A2
Deng, L.-C., Newberg, H. J., Liu, C., et al. 2012, RAA, 12, 735
Finkbeiner, D. P., Schlafly, E. F., Schlegel, D. J., et al. 2016, ApJ, 822, 66
Fukugita, M., Ichikawa, T., Gunn, J. E., et al. 1996, AJ, 111, 1748
Gaia Collaboration, Brown, A. G. A., Vallenari, A., et al. 2018, A&A, 616, A1
Gaia Collaboration, Brown, A. G. A., Vallenari, A., et al. 2021a, A&A, 649, A1
Gaia Collaboration, Brown, A. G. A., Vallenari, A., et al. 2021b, A&A, 650, C3
Gaia Collaboration, Montegriffo, P., Bellazzini, M., et al. 2023, A&A, 674, A33
Gaia Collaboration, Vallenari, A., Brown, A. G. A., et al. 2023, A&A, 674, A1
High, F. W., Stubbs, C. W., Rest, A., et al. 2009, AJ, 138, 110
Huang, B., & Yuan, H. 2022, ApJS, 259, 26
Huang, B., Yuan, H., Xiang, M., et al. 2024, ApJS, 271, 13
Huang, Y., Yuan, H., Li, C., et al. 2021, ApJ, 907, 68
Ivezić, Ž., Smith, J. A., Miknaitis, G., et al. 2007, AJ, 134, 973
Koleva, M., & Vazdekis, A. 2012, A&A, 538, A143
Landolt, A. U. 1992, AJ, 104, 372
Landolt, A. U. 2009, AJ, 137, 4186
Landolt, A. U. 2013, AJ, 146, 131
Liu, X.-W., Yuan, H.-B., Huo, Z.-Y., et al. 2014, in IAU Symp. 298, Setting the Scene for Gaia and LAMOST, ed. S. Feltzing et al. (Cambridge: Cambridge Univ. Press), 310
López-Sanjuan, C., Varela, J., Cristóbal-Hornillos, D., et al. 2019, A&A, 631, A119
Luo, A.-L., Zhao, Y.-H., Zhao, G., et al. 2015, RAA, 15, 1095
Mendes de Oliveira, C., Ribeiro, T., Schoenell, W., et al. 2019, MNRAS, 489, 241
Montegriffo, P., De Angeli, F., Andrae, R., et al. 2023, A&A, 674, A3
Niu, Z., Yuan, H., & Liu, J. 2021a, ApJ, 909, 48
Niu, Z., Yuan, H., & Liu, J. 2021b, ApJL, 908, L14
Niu, Z., Yuan, H., Wang, S., et al. 2021c, ApJ, 922, 211
Oke, J. B., & Gunn, J. E. 1983, ApJ, 266, 713
Padmanabhan, N., Schlegel, D. J., Finkbeiner, D. P., et al. 2008, ApJ, 674, 1217
Riello, M., De Angeli, F., Evans, D. W., et al. 2021, A&A, 649, A3
Schlegel, D. J., Finkbeiner, D. P., & Davis, M. 1998, ApJ, 500, 525
Stetson, P. B. 2000, PASP, 112, 925
Sun, Y., Yuan, H., & Chen, B. 2022, ApJS, 260, 17
Thanjavur, K., Ivezić, Ž., Allam, S. S., et al. 2021, MNRAS, 505, 5941
Tonry, J. L., Stubbs, C. W., Lykke, K. R., et al. 2012, ApJ, 750, 99
Wolf, C., Onken, C. A., Luvaul, L. C., et al. 2018, PASA, 35, e010
Wu, Y., Luo, A.-L., Li, H.-N., et al. 2011, RAA, 11, 924
Xiao, K., & Yuan, H. 2022, AJ, 163, 185
Xiao, K., Yuan, H., Huang, B., et al. 2023a, ChSBu, 68, 2790
Xiao, K., Yuan, H., Huang, B., et al. 2023b, ApJS, 268, 53
Xiao, K., Yuan, H., Lopez-Sanjuan, C., et al. 2023c, ApJS, 269, 58
Yang, L., Yuan, H., Zhang, R., et al. 2021, ApJL, 908, L24
York, D. G., Adelman, J., Anderson, J. E., et al. 2000, AJ, 120, 1579
Yuan, H., Liu, X., Xiang, M., et al. 2015, ApJ, 799, 133
Yuan, H. B., Liu, X. W., & Xiang, M. S. 2013, MNRAS, 430, 2188
Zhang, R., & Yuan, H. 2020, ApJL, 905, L20
Zhao, G., Zhao, Y.-H., Chu, Y.-Q., et al. 2012, RAA, 12, 723
Zheng, J., Zhao, G., Wang, W., et al. 2018, RAA, 18, 147
Zheng, J., Zhao, G., Wang, W., et al. 2019, RAA, 19, 003